JOURNAL OF GEOPHYSICAL RESEARCH, VOL. 115, A00F08, doi:10.1029/2009JA014619, 2010

Origin of energetic electron precipitation >30 keV into the atmosphere

Mai Mai Lam,[1] Richard B. Horne,[2] Nigel P. Meredith,[2] Sarah A. Glauert,[2] Tracy Moffat-Griffin,[2] and Janet C. Green[3]

Received 3 July 2009; revised 13 October 2009; accepted 17 November 2009; published 20 April 2010.

[1] Energetic electrons are deposited into the atmosphere from Earth's inner magnetosphere, resulting in the production of odd nitrogen (NO_x). During polar night, NO_x can be transported to low altitudes, where it can destroy ozone, affecting the atmospheric radiation balance. Since the flux of energetic electrons trapped in the magnetosphere is related to solar activity, the precipitation of these electrons into Earth's atmosphere provides a link between solar variability and changes in atmospheric chemistry which may affect Earth's climate. To determine the global distribution of the precipitating flux, we have built a statistical model binned by auroral electrojet (*AE*) index, magnetic local time (MLT), and *L* shell of $E > 30$ keV precipitating electrons from the Medium Energy Proton and Electron Detector (MEPED) on board the NOAA Polar Orbiting Environmental Satellites (POES) low-altitude satellites NOAA-15, NOAA-16, NOAA-17, and NOAA-18. We show that the precipitating flux increases with geomagnetic activity, suggesting that the flux is related to substorm activity. The precipitating fluxes maximize during active conditions where they are primarily seen outside of the plasmapause on the dawnside. The global distribution of the precipitating flux of $E > 30$ keV electrons is well-correlated with the global distribution of lower-band chorus waves as observed by the plasma wave experiment onboard the Combined Release and Radiation Effects Satellite (CRRES) satellite. In addition, the electron precipitation occurs where the pitch angle diffusion coefficient due to resonant interaction between electrons and whistler mode chorus waves is high, as calculated using the pitch angle and energy diffusion of ions and electrons (PADIE) code. Our results suggest that lower-band chorus is very important for scattering >30 keV electrons from Earth's inner magnetosphere into the atmosphere.

Citation: Lam, M. M., R. B. Horne, N. P. Meredith, S. A. Glauert, T. Moffat-Griffin, and J. C. Green (2010), Origin of energetic electron precipitation >30 keV into the atmosphere, *J. Geophys. Res.*, *115*, A00F08, doi:10.1029/2009JA014619.

1. Introduction

[2] Energetic electron precipitation from the Earth's magnetosphere into the atmosphere has become recognized as an important process affecting the chemistry of the upper atmosphere. Precipitating electrons produce forms of odd nitrogen (NO_x) which undergo a series of chemical reactions that deplete ozone [e.g., *Thorne*, 1977] and affect the radiation budget of the upper atmosphere. At high altitudes, NO_x has a short lifetime in sunlight due to photodissociation, but if it can be produced in darkness and transported downward to the stratosphere, or produced in the stratosphere directly, the lifetime is much longer [*Solomon et al.*, 1982] and the potential for ozone destruction is much higher. The polar regions are particularly important in this respect. The region poleward of 40° invariant latitude corresponds to the highest electron precipitation region [*Gaines et al.*, 1995]. NO_x produced inside the polar vortex during winter can be transported downward into the stratosphere to 35–40 km [*Siskind et al.*, 2000; *Randall et al.*, 2005, 2006; *Clilverd et al.*, 2007] where it can accumulate. Up to 60% ozone depletion at 35–40 km has been attributed to energetic electron precipitation [*Randall et al.*, 2005], and atmospheric circulation models show that this can result in a reduction of temperature of up to 2 K in the polar regions, and up to 0.5 K at mid latitudes [*Rozanov et al.*, 2005]. As NO_x produced by energetic electron precipitation is more frequent and persistent than that produced by solar proton events [*Randall et al.*, 2005], electron precipitation from the Earth's inner magnetosphere could be very important for communicating solar variability to the Earth's middle atmosphere [e.g., *Kozyra et al.*, 2006].

[3] There is a large uncertainty as to which energy range of precipitating electrons is more important in terms of their effects on stratospheric chemistry. Lower-energy electrons

[1]Department of Physics and Astronomy, University of Leicester, Leicester, UK.
[2]British Antarctic Survey, Natural Environment Research Council, Cambridge, UK.
[3]Space Weather Prediction Center, National Oceanic and Atmospheric Administration, Boulder, Colorado, USA.

0148-0227/10/2009JA014619

Table 1. NOAA POES Satellites Used in This Study[a]

Satellite	Altitude (km)	Inclination Angle (°)	Period (min)	LTAN	Data Window
NOAA-15	807	98.5	101.1	1650	01/07/98–31/12/07
NOAA-16	849	99.0	102.1	1731	10/01/01–31/12/07
NOAA-17	810	98.7	101.2	2134	12/07/02–31/12/07
NOAA-18	854	98.7	102.1	1341	07/06/05–31/12/07

[a]Columns are satellite name, altitude, inclination angle, orbital period, local time of the ascending node (LTAN), and the intervals of the data used in this study. POES, Polar Orbiting Environmental Satellites.

(1–10 keV) penetrate down to 100 km or so whereas 10–100 keV electrons deposit most of their energy at altitudes in the range 75–100 km. Much higher energy 0.1–1 MeV electrons, associated with the Van Allen radiation belts, penetrate to lower altitudes of 55–75 km [e.g., *Gaines et al.*, 1995]. In general the flux of precipitating electrons decreases rapidly with increasing energy and it is not yet clear whether NO_x produced at high altitudes by lower-energy electrons, which requires substantial downward transport, is more important than NO_x produced at lower altitudes by higher-energy electrons. Observations suggest both are important under different conditions [*Clilverd et al.*, 2007, 2009].

[4] While there have been several statistical studies of electron precipitation in the 1–10 keV energy range at low altitudes, [e.g., *Fuller-Rowell and Evans*, 1987; *Roble and Ridley*, 1987; *Newell et al.*, 1996a, 1996b; *Hardy et al.*, 2008], statistical surveys of precipitating electrons at higher energies are more difficult. This is partly due to the lack of energy coverage by particle detectors on low-altitude satellites measuring inside the loss cone, the restricted latitude coverage of satellites such as UARS and DEMETER, and the difficulty of measuring low precipitating flux at MeV energies inside the loss cone.

[5] Nevertheless there are numerous observations of electron precipitation at higher energies. *Millan and Thorne* [2007] give a comprehensive review of radiation belt electron losses including losses due to precipitation into the atmosphere. Balloon experiments up to ~300 keV show that microbursts are the main form of electron precipitation on the dayside [*Parks*, 1978]. SAMPEX satellite observations show that relativistic microburst precipitation is important during geomagnetic storms [*Blake et al.*, 1996; *Lorentzen et al.*, 2001a, 2001b; *O'Brien and McPherron*, 2003; *O'Brien et al.*, 2004; *Thorne et al.*, 2005]. On the duskside, relativistic precipitation associated with scattering by EMIC waves has been observed using X-ray observations from balloons [*Foat et al.*, 1998; *Lorentzen et al.*, 2000; *Millan et al.*, 2002] and using SAMPEX [e.g., *Bortnik et al.*, 2006]. There have also been observations of lightning-induced electron precipitation from the Earth's radiation belts in the ~1–300 keV range [*Voss et al.*, 1984, 1998; *Inan et al.*, 2007, and references therein].

[6] In one particular study of electron precipitation >30 keV it was noted that the distribution in magnetic local time (MLT) is somewhat different to that for <10 keV, particularly in the premidnight MLT sector [*Codrescu et al.*, 1997]. This could be due to an energy dependency in the mechanism of production of precipitation, or to an energy dependency of the mechanism of transport of the source particles. For example, intense electron precipitation <10 keV is associated with auroral acceleration processes which may occur on magnetic field lines extending into the magnetotail, and which may overlap with a much broader region of diffuse precipitation extending equatorward caused by wave-particle interactions near the magnetic equator. Above 30 keV, and extending up to several MeV, the precipitation is more likely to be associated with wave-particle interactions in the Van Allen radiation belts which act on different timescales and different MLT regions. Possible candidates include precipitation by whistler mode chorus, plasmaspheric hiss and electromagnetic ion cyclotron waves.

[7] In view of the importance of energetic electron precipitation for atmospheric chemistry, the purpose of this paper is to determine the statistical distribution of >30 keV electron precipitation and the wave-particle interactions that are most likely responsible. We present a global model of the $E > 30$ keV flux of precipitating electrons as a function of geomagnetic activity using data from four NOAA Polar Orbiting Environmental Satellites (POES) (section 2). Since whistler mode chorus waves are known to scatter electrons in this energy range (section 3) we compare the results with an activity-dependent global model of lower-band chorus wave intensities derived from the Combined Release and Radiation Effects Satellite (CRRES) (section 3). We examine the associated resonant energies and bounce-averaged diffusion coefficients at the edge of the loss cone (section 4) and perform a correlation analysis (section 5) to investigate the relationship between the waves and the precipitating electrons. The results are then compared with the absorption measured by the Halley IRIS (section 6). The results of our study are discussed in section 7 and the conclusions presented in section 8.

2. Electron Precipitation >30 keV

[8] The particle data used in this study were collected by the Medium Energy Proton and Electron Detector (MEPED) on board the NOAA POES. These satellites orbit the Earth approximately 14 times each day in Sun-synchronous, low-altitude, polar orbits. Here we use data from NOAA-15, NOAA-16, NOAA-17, and NOAA-18 (Table 1).

[9] The MEPED instrument includes two electron solid-state detector telescopes, each with a field of view of 30°, that measure the flux of electrons in three energy bands in the range 30 keV to 2,500 keV. One, called the '0°' telescope, is aligned such that the center of its field of view is rotated 9° from the direction outward along the local zenith. The other, called the '90°' telescope, is mounted perpendicular to the '0°' telescope. The center axis of its field of view is rotated 9° from the direction antiparallel to the direction of the spacecraft velocity. These rotations ensure a clear field of view. In this study electron data from the $E >$

30 keV channel are used. Data from each detector are accumulated for 1 s and, since the electronics are shared between the two detectors, a full data set from both requires 2 s to acquire.

[10] The $E > 30$ keV electron channel not only responds to electrons, but also to ring current protons in the energy range $210 < E < 2700$ keV. Using the MEPED proton telescopes, which directly monitor the proton flux in six energy bands in the range 30 keV to 6,900 keV, a first-order correction was applied to the data to remove the protons. Even for geomagnetically active conditions, but excluding solar proton events, the peak average precipitating proton flux in the range 80–240 keV was 2 orders of magnitude lower than the peak average precipitating electron flux and thus we conclude that any error introduced by this process was small. Details of the correction procedure are given in Appendix A.

[11] Solar proton events, which may also contaminate the electron channels, were removed using the NOAA Space Environment Center catalogue of solar proton events affecting the Earth's environment. Start dates were taken directly from the catalogue and the end dates were determined from the time when the GOES-8 Space Environment Monitor $E > 10$ MeV flux fell below 10 $cm^{-2}s^{-1}sr^{-1}$. Data during these periods were removed.

[12] The trapped electron flux is usually much greater than the precipitating flux. Therefore, to obtain an accurate measure of the precipitating flux it is important to select data from the '0°' telescope only when it is measuring electrons inside the loss cone. To do this the local pitch angle at the satellite, corresponding to the edge of the loss cone α_{satLC}, was determined by assuming conservation of the first adiabatic invariant

$$\alpha_{satLC} = \sin^{-1}\left(\sqrt{\frac{B_{sat}}{B_{120}}}\right) \quad (1)$$

where B_{sat} is the ambient magnetic field at the spacecraft and B_{120} is the ambient magnetic field at the "foot of the field line," i.e., the point where the magnetic field threading the satellite intersects ~120 km in altitude above Earth. The magnetic field vector both at the satellite and at the foot of the field line was calculated using the International Geomagnetic Reference Field (IGRF) model for halfway through the year in question. Since the MEPED detectors have a finite opening angle of ±15° precipitating particles were selected using the condition

$$\alpha_{sat} + 15^\circ < \alpha_{satLC} \quad (2)$$

where α_{sat} is the particle pitch angle at the satellite. The field of view of the '0°' telescope typically lies completely within the bounce loss cone for $L > \sim 1.4$ [*Rodger et al.*, 2010].

[13] Since the electron flux falls rapidly with increasing energy the electron telescope sensor was checked to ensure the counts in the $E > 30$ keV channels were greater than or equal to those in the $E > 100$ keV channel, and similarly, that the counts for $E > 100$ keV channels were greater than or equal to those in the $E > 300$ keV channel. The precipitating electron flux was then binned as a function of McIlwain L shell and MLT in steps of 0.1 L and 1 h MLT for each of the four satellites. The McIlwain L shell is calculated using the IGRF model of the magnetic field and the National Space Science Data Center INVAR program.

[14] The global morphology of the precipitating electron flux $E > 30$ keV is shown as a function of L, MLT and geomagnetic activity in Figures 1a–1c. The results are shown for quiet ($AE < 100$ nT), moderate ($100 < AE < 300$ nT), and active ($AE > 300$ nT) geomagnetic conditions as measured by the AE index in Figures 1a–1c, respectively. During quiet conditions (Figure 1a) the precipitating flux is low and generally less than 2×10^4 cm^{-2} s^{-1} sr^{-1}. The flux tends to be largest for $L \geq 6$, at night between 2000–0300 MLT, and on the dayside between 0500–1700 MLT. However, as magnetic activity increases the precipitating flux increases substantially from just before midnight, through dawn to the afternoon sector. During active conditions $AE > 300$ nT the precipitating flux extends to lower L and over a larger range of MLT with fluxes exceeding 5×10^5 cm^{-2} s^{-1} sr^{-1} for $L > 4$ from 2100 MLT through dawn to 1200 MLT.

3. Source of Electron Precipitation

[15] The fact that the region of electron precipitation extends to as low as $L = 4$ during very active conditions suggests that there may be a number of sources, and hence a number of mechanisms responsible for the precipitation. One of the most well known types of precipitation is that associated with the discrete aurora, but this is usually due to 1–10 keV electrons [e.g., *Fuller-Rowell and Evans*, 1987; *Newell et al.*, 1996a, 1996b] which have been accelerated above the ionosphere on auroral field lines. This is somewhat lower in energy than that discussed here. Since the MLT distribution of the precipitation is consistent with injection and transport of >30 keV electrons from the nightside through dawn to the dayside under the action of convection electric fields, precipitation by wave-particle interactions operating near the magnetic equatorial region appears to be more likely. There are a number of candidates. Electrostatic waves generally resonate and scatter electrons in the 0.1–10 keV energy range [e.g., *Horne and Thorne*, 2000] are therefore too low in energy. On the other hand, electromagnetic ion cyclotron waves generally resonate with >500 keV electrons which appears too high in energy [*Horne and Thorne*, 1998; *Summers and Thorne*, 2003; *Jordanova et al.*, 2008; *Miyoshi et al.*, 2008].

[16] *Meredith et al.* [2004] show plasmaspheric hiss generally scatters electrons in the 20 keV to 2 MeV energy range, so hiss is a possible candidate. During active conditions, equatorial hiss ($|MLAT| < 15°$) is seen from 0600 to 2100 MLT and midlatitude hiss from 0800 to 1800 MLT and mostly confined to the plasmasphere ($2 < L < 4$). Hiss does extend out beyond $L = 6$ in high-density plumes [*Meredith et al.*, 2004; *Summers et al.*, 2008], however this tends to be confined to the postnoon sector. Plasmaspheric hiss is therefore not in the right location to be the source of the electron precipitation examined in this paper.

[17] Whistler mode chorus waves resonate with electrons over a wide range of energies, from a few hundred eV up to several MeV [e.g., *Horne et al.*, 2005] and thus appear to be the most favorable candidate. The emissions are often

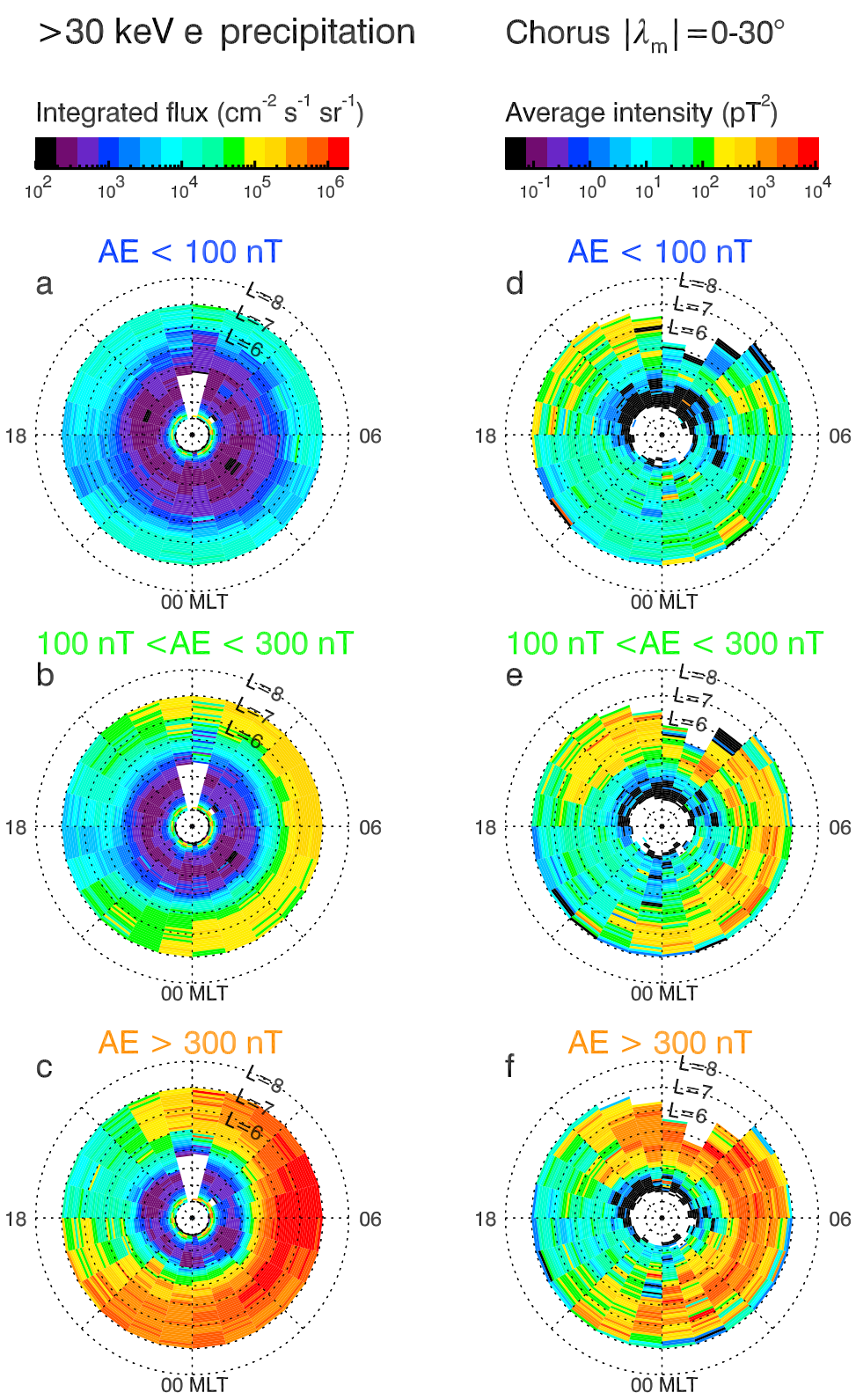

Figure 1. (left) The average flux of precipitating electrons with $E > 30$ keV as a function of L and magnetic local time for (a) quiet ($AE < 100$ nT), (b) moderate ($100 < AE < 300$ nT), and (c) active ($AE > 300$ nT) conditions. (right) The average lower-band chorus in over the magnetic latitude range $|\lambda_m| < 30°$ as a function of L and magnetic local time for (d) quiet ($AE < 100$ nT), (e) moderate ($100 < AE < 300$ nT), and (f) active ($AE > 300$ nT) conditions. Each plot extends out to $L = 8$ with noon at the top and dawn to the right.

observed in two distinct bands, referred to as upper ($0.5 f_{ce} < f < f_{ce}$) and lower ($0.1 f_{ce} < f < 0.5 f_{ce}$) band chorus, with a gap at $0.5 f_{ce}$ [*Tsurutani and Smith*, 1974; *Santolík et al.*, 2004]. Both bands are substorm-dependent and emissions intensify during active conditions [*Tsurutani and Smith*, 1977; *Meredith et al.*, 2001; *Miyoshi et al.*, 2003]. Electrons with energies of the order of 1 keV or so tend to resonate with upper band chorus [*Inan et al.*, 1992; *Johnstone et al.*, 1993]. At higher energies, lower-band chorus provides more effective scattering, especially near the loss cone [*Ni et al.*, 2008].

[18] To test whether whistler mode chorus waves could be the source of electron precipitation observed here we analyzed data from the plasma wave experiment on board the CRRES [*Johnson and Kierein*, 1992]. This instrument measured electric fields from 5.6 Hz to 400 kHz, using a 100 m tip-to-tip long wire antenna [*Anderson et al.*, 1992]. Chorus electric field spectral intensities were first converted to magnetic field spectral intensities, as described by *Meredith et al.* [2003]. Since energetic electrons interact most readily with lower-band chorus ($0.1 < f/f_{ce} < 0.5$) [*Horne and Thorne*, 1998], the derived wave spectral intensity ($pT^2\ Hz^{-1}$) was integrated over this frequency range to obtain the lower-band chorus magnetic field intensity, B_w^2, where B_w is the wave magnetic field amplitude. B_w^2 together with the ratio f_{pe}/f_{ce}, were then rebinned as a function of half-orbit (outbound or inbound) and L in steps of 0.1 L. For more detailed spectral analysis the wave magnetic field intensities from $0.1 f_{ce}$ to f_{ce} were rebinned in steps of $0.1 f_{ce}$ at the same spatial resolution. The wave data were recorded together with the time in UT, magnetic latitude (λ_m), MLT and time spent in each bin at the same resolution. The L value and magnetic latitude were determined using the Olson-Pfitzer tilt-dependent static model [*Olson and Pfitzer*, 1977] and the IGRF 85 model.

[19] Figures 1d–1f show the global morphology of lower-band chorus magnetic field wave intensities in the equatorial region, averaged over the magnetic latitude range $|\lambda_m| < 30°$, as a function of L, MLT and geomagnetic activity. Wave intensities increase with substorm activity similar to the precipitating flux. The MLT distribution of the waves for medium and active conditions is also very similar to that for the precipitating flux, and both precipitation and wave power extend to lower L ($L \approx 4$) for increasing AE. During active conditions (Figure 1f) the wave intensity typically exceeds 1000 pT^2 for $L > 4$ from 2100 MLT through dawn to 1500 MLT. This qualitative agreement suggests that resonant pitch angle scattering of electrons by lower-band chorus could be a very important source of $E > 30$ keV electron precipitation into Earth's atmosphere.

4. Electron Pitch Angle Diffusion

4.1. Resonant Energies

[20] The waves shown in Figure 1 span a range of frequencies and latitudes near the magnetic equator. Ideally it would be desirable to measure the precipitating electron flux near the equator that is directly associated with these waves and compare it to that observed by POES at the foot of the field line. Unfortunately the size of the loss cone near the equator is so small (typically 5° degrees at $L = 4$) that it cannot be resolved by particle detectors. However, for a given band of waves we can determine the range of resonant energies that can be scattered efficiently by the waves, or alternatively, for a given electron energy range we can determine the range of resonant frequencies and test how well these correspond to the frequency at which wave power maximizes. Here we assume that the scattering can be treated as a diffusion problem where the electrons interact with a series of uncorrelated waves, but note that chorus waves also undergo nonlinear wave-particle interactions which have yet to be fully assessed [e.g., *Omura et al.*, 2007].

[21] Electron diffusion by the waves is most effective when the resonance condition is satisfied

$$\omega - k_{\|} v_{\|} + n|\Omega_e|/\gamma = 0 \tag{3}$$

where ω is the (angular) wave frequency, Ω_e is the electron cyclotron frequency ($|\Omega_e| = 2\pi f_{ce}$), $k_{\|}$ is the wave number parallel to the ambient magnetic field B_0, $\gamma = (1 - v^2/c^2)^{-1/2}$, $v^2 = v_{\perp}^2 + v_{\|}^2$, $v_{\perp}$ and $v_{\|}$ are the electron velocities perpendicular and parallel to B_0, and n is the harmonic number. For whistler mode waves $\omega < |\Omega_e|$, and so for parallel propagation along B_0, resonance is possible when the wave frequency is Doppler-shifted up in frequency to the cyclotron frequency. For propagation along the magnetic field, with the convention that $\Omega_e < 0$, the resonance with the lowest resonant energy is $n = -1$. The resonance condition is then an ellipse in velocity space and the minimum resonant energy is obtained from the point where the ellipse touches the $v_{\perp} = 0$ axis. The wave number, $k_{\|}$, is determined by solving the cold plasma dispersion relation for whistler mode waves propagating parallel to the magnetic field, which, for an electron-proton plasma is given by [e.g., *Walker*, 1993]

$$\frac{c^2 k_{\|}^2}{\omega^2} = 1 - \frac{\omega_{pe}^2}{\omega(\omega - |\Omega_e|)} - \frac{\omega_{pi}^2}{\omega(\omega + \Omega_p)} \tag{4}$$

where Ω_p is the proton cyclotron frequency, ω_{pe} and ω_{pi} are the electron and proton plasma frequencies. For a given electron kinetic energy, E, the electron velocity is given by $v = c\sqrt{E(E + 2E_0)}/(E + E_0)$ where $E_0 = m_0 c^2$ and m_0 is the electron rest mass.

[22] A representative example of the waves and the precipitation for active magnetic conditions is shown in Figure 2 for $L = 5.05$. Figures 2a and 2b show the average equatorial ($|\lambda_m| < 15°$) and midlatitude ($15° < |\lambda_m| < 30°$) chorus wave magnetic field intensities as a function of normalized frequency and MLT. The frequency for resonance with 30 keV electrons (from here on referred to as the resonant frequency) is shown by the black line in Figures 2a and 2b. Waves at lower frequencies resonate with >30 keV electrons. Figure 2d shows the ratio f_{pe}/f_{ce}. For the calculations in this paper we have averaged f_{pe} and f_{ce} over the appropriate latitude ranges.

[23] In computing the resonant frequency the measured electron plasma frequency, averaged over the appropriate latitude range, was used. Between 2200 and 1400 MLT the resonant frequency lies in the range of strong equatorial

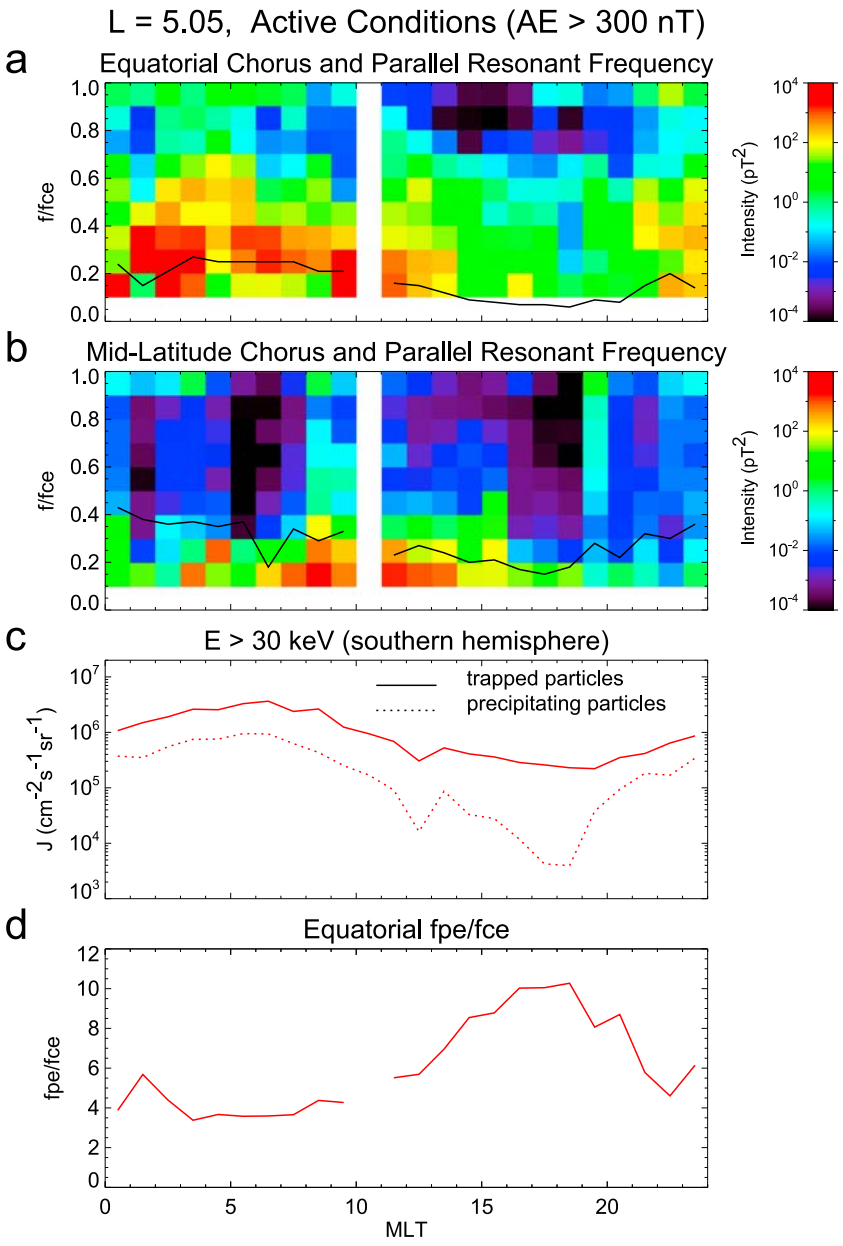

Figure 2. A representative example of the waves and the precipitation for active magnetic conditions is shown in Figure 2 for $L = 5.05$. Wave and particle data as a function of magnetic local time (MLT) during active conditions at $L = 5.05$. (a) The intensity of equatorial lower-band chorus as a function of the frequency f normalized to the electron gyro frequency f_{ce}, (b) the intensity of midlatitude lower-band chorus during active conditions as a function of the frequency f normalized to the electron gyro frequency f_{ce}, (c) the trapped $E > 30$ keV electron flux (solid lines) and the precipitating $E > 30$ keV electron flux (dotted lines), and (d) the ratio of electron plasma frequency to the electron gyro frequency f_{pe}/f_{ce}. The black trace in Figures 2a and 2b represents the resonant frequency for precipitating 30 keV electrons.

chorus (Figure 2a) wave power but falls below 0.1 f_{ce} on the dusk side between 1600 and 2200 MLT. The reduction in frequency on the dusk side is mainly due to the higher electron plasma frequency in this region. At mid latitudes (Figure 2b) the resonant frequency is higher than that at the equator, due to the higher background magnetic field, and lies in the region of strong mid latitude chorus between 0600 and 1400 MLT. Thus both equatorial and mid latitude waves can both contribute to electron diffusion for $E \geq$ 30 keV into the loss cone and hence precipitation. It is also clear that there is strong wave power at frequencies above the resonant frequency, particularly near dawn, and that this can contribute to diffusion of <30 keV electrons.

[24] Figure 2c shows the trapped and precipitating electron flux measured at the same L by POES near the foot of the magnetic field line. The trapped flux always dominates the precipitating flux, by a factor of 5 or more, indicating that electron diffusion into the loss cone is a result of weak

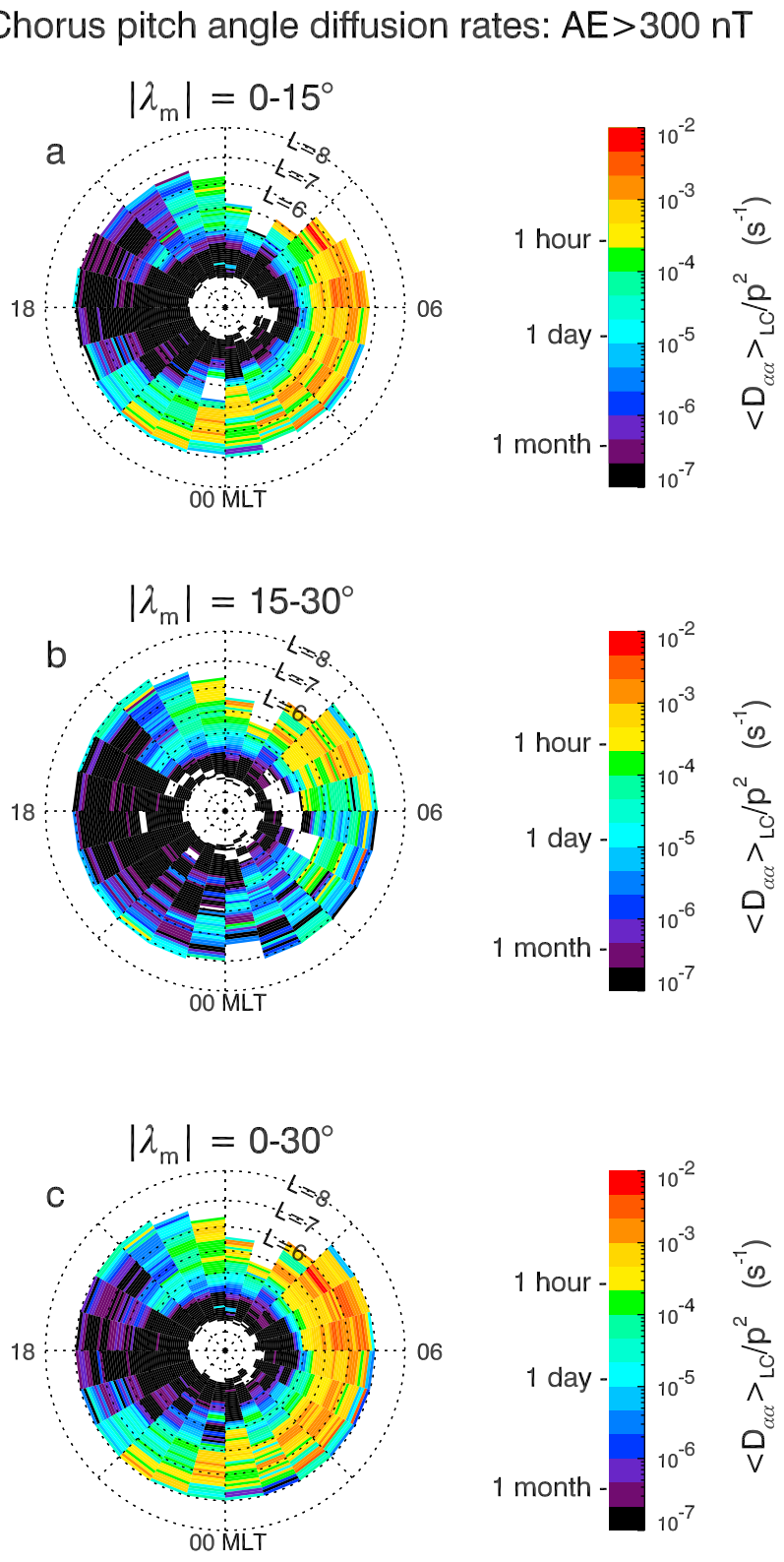

Figure 3. The bounce-averaged pitch angle diffusion coefficient for 30 keV at the edge of the loss cone ($\langle D_{\alpha\alpha}\rangle_{LC}/p^2$) as a function of L and magnetic local time during active conditions for (a) equatorial ($|\lambda_m| < 15°$) chorus, (b) midlatitude ($15° < |\lambda_m| < 30°$) chorus, and (c) a combination of equatorial and midlatitude chorus. Each plot extends out to $L = 8$ with noon at the top and dawn to the right.

turbulence, and not strong diffusion which fills the loss cone and would result in approximately equal trapped and precipitating flux. It is interesting to note that the trapped flux peaks near dawn and has a minimum near 1900–2000 MLT. This is discussed later. The precipitating flux tends to follow the trend in the trapped flux, and is high in the region where the resonant frequency overlaps with strong lower-band chorus wave intensity, but is much lower than the trapped flux in the afternoon sector where the lower-band chorus wave power is low, and the resonant frequency is low. Since electron diffusion is proportional to wave power this variation supports the link between the waves and the precipitating flux. It should be noted that at an altitude of ~800 km, the perpendicular fluxes are only barely trapped and are sometimes located in the drift loss cone. Mapped to the equator, this represents a pitch angle range which is only slightly above the loss cone and may not be representative of the true trapped population.

4.2. Pitch Angle Diffusion Rates

[25] Although the waves can resonate with the electrons in the appropriate energy range, this does not ensure that the waves diffuse electrons into the loss cone. Wave-particle interactions diffuse electrons in pitch angle and energy in such a way as to reduce the gradients in the electron distribution function. In the equatorial region the electron distribution usually falls rapidly with energy and contains a gradient in pitch angle due to the presence of the loss cone [e.g., *Horne et al.*, 1987]. However, pitch angle diffusion does not always extend into the loss cone, for example, magnetosonic waves, which can occur in the same frequency range as parallel propagating whistler mode waves, only scatter electrons at very large pitch angles and thus do not contribute to precipitation directly [*Horne et al.*, 2007]. Furthermore, pitch angle diffusion depends on several properties of the waves, such as the direction of propagation, the bandwidth, wave intensity and latitude distribution of the waves. To establish whether lower-band chorus waves diffuse electrons into the loss cone effectively, here we present pitch angle diffusion coefficients calculated at 30 keV at the edge of the loss cone. Of course the precipitation flux depends on both the diffusion rates and the gradients at the edge of the loss cone, but in the absence of detailed particle measurements the diffusion coefficients are used here as a proxy.

[26] The pitch angle and energy diffusion of ions and electrons (PADIE) code [*Glauert and Horne*, 2005] was used to calculate bounce-averaged pitch angle diffusion rates. Bounce averaging takes into account the latitudinal distribution of the waves and the interactions between the waves and electrons as electrons travel along the magnetic field line between mirror points in the northern and southern hemispheres. The code assumes that the wave intensity can be described by a Gaussian distribution, and that the distribution of wave normal angles, i.e., the wave propagation direction, is Gaussian in $X = \tan \psi$, where ψ is the angle between the magnetic field direction and the k vector of the waves. The wave parameters are based on those used before for studying lower-band whistler mode chorus, and which were obtained from analyzing whistler mode data [*Meredith et al.*, 2002; *Horne et al.*, 2005] and used in global simulation models [*Varotsou et al.*, 2005, 2008; *Fok et al.*, 2008; *Albert et al.*, 2009]. Maximum wave power was set to a frequency of $0.35f_{ce}$, with a bandwidth of $0.15f_{ce}$, and lower and upper cutoffs at $0.125f_{ce}$ and $0.575f_{ce}$ outside which wave power is set to zero. The distribution of wave normal angles is set with a peak at $X = \tan 0°$ with an angular spread of $X_w = \tan 30°$. An electron-proton plasma was assumed and Landau $n = 0$ and $n = \pm 1, \pm 2, .. \pm 5$ cyclotron harmonic interactions were included. Higher-order resonances were small by comparison. The appropriate values of f_{pe}/f_{ce} were selected according to the data at each L shell and MLT, and the diffusion rates, which are proportional to wave intensity, were scaled by the observed wave intensity in each data bin corresponding to $0.1L$ and 1 h MLT. Since chorus tends to be restricted to within ±15° of the magnetic equator on the nightside whereas dayside chorus extends to ±30° and beyond, the bounce averaged pitch angle diffusion coefficients $\langle D_{\alpha\alpha}\rangle_{LC}/p^2$ at the edge of the loss cone were calculated separately for equatorial ($|\lambda_m| < 15°$) and midlatitude chorus ($15° < |\lambda_m| < 30°$).

[27] Figure 3 shows the bounce-averaged diffusion rates at 30 keV for active magnetic conditions. For equatorial chorus (Figure 3a) diffusion rates peak near dawn near L = 5–6 and typically exceed 2×10^{-4} s^{-1} over a wide range of MLT 2300–0900 MLT for $L > 4.5$. At mid latitudes (Figure 3b) diffusion rates are strongest on the dayside which largely reflects the MLT distribution of the waves (compare with Figures 2a and 2b). When both equatorial and mid latitude diffusion rates are combined (Figure 3c) pitch angle diffusion into the loss cone is possible for a wide range of L and MLT, comparable to that observed for electron precipitation (Figure 1c).

5. Correlation Analysis

[28] If lower-band chorus is largely responsible for the precipitation of $E > 30$ keV electrons, then there should be a significant correlation between the diffusion rates and the $E > 30$ keV precipitating electron flux. To try to quantify this relation, Figure 4a shows the Pearson correlation coefficient r between the logarithm of the $E > 30$ keV electron precipitating flux and the logarithm of $\langle D_{\alpha\alpha}\rangle_{LC}/p^2$. This has been done for high geomagnetic activity, i.e., $AE > 300$ nT. Figure 4b shows the minimum value of the confidence interval for the correlation values (see Appendix B for more details).

[29] When the correlation is calculated for all MLT (black line) the correlations values are significant (minimum confidence interval of 95%) for $L > 4.7$ (black diamonds). The correlation is large ($r > 0.8$) for $L > 5.1$, and drops to lower values for $L \leq 5.1$.

[30] Similar large correlations ($r > 0.8$) are obtained for $L > 5.1$ when the data are split into dayside (purple) and nightside (green) sectors. The correlation on the nightside is $r = 0.5$ at $L = 4$ with at least a 95% confidence interval. As L decreases below 5.1, the dayside correlation becomes increasingly smaller than that on the nightside which may indicate that the correlation for $L < 5$ is much higher on the nightside than the dayside (unfortunately the minimum confidence interval for dayside correlation drops below 95% for $L < 4.7$).

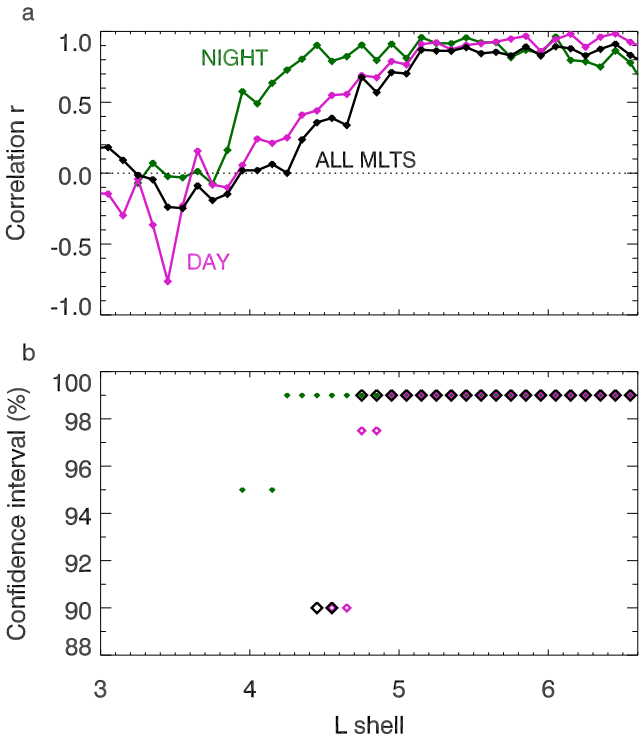

Figure 4. (a) The variation of the Pearson correlation coefficient between the log of the $E > 30$ keV precipitating flux and the log of $\langle D_{\alpha\alpha}\rangle_{LC}/p^2$ for lower-band chorus during active conditions as a function of L for all MLT (black trace), the nightside (green trace), and the dayside (purple trace) and (b) the minimum confidence interval for each correlation.

[31] When the correlation is performed over $3 < L < 6.6$, and presented as a function of MLT (Figure 5a), the correlation exceeds 0.8 between 0200–1100 MLT, and is even higher near dawn (>0.95 between 0500 and 0800 MLT) before dropping in the afternoon sector. The minimum confidence intervals are 95% or greater (except at 15.5 MLT).

6. Ionospheric Absorption

[32] Ground-based riometers provide an alternative measure of $E > 40$ keV electron precipitation by measuring the absorption of cosmic radio noise [*Collis et al.*, 1984]. As radio signals propagate through the ionosphere electron precipitation increases ionization and the collision frequency which leads to absorption of the signal. The method is most sensitive to electron precipitation of a few tens of keV in the altitude region 70–110 km, and has been well established [*Hargreaves*, 1979]. The absorption of cosmic radio noise at Halley Research station (75° 35′ S, 26°34′ W) has been found to depend on the *AE* index and MLT, with the highest absorption occurring in the 0400–1600 MLT sector for $AE >$ 140 nT, and in the 1200–2000 MLT sector for $AE \leq 140$ nT [*Rosenberg and Dudeney*, 1986]. The British Antarctic Survey have operated an imaging riometer for ionospheric studies (IRIS) at Halley Research Station for several years. Since the Halley Research Station is located at $L \sim 4.3$ we can use Halley IRIS data to provide an independent measure of electron precipitation.

[33] The Halley IRIS operated at 38.2 MHz, and recorded data at 1 s resolution. In order to provide high spatial resolution we selected data from the central beam of the 49 beams which had a viewing angle of 11° corresponding to a circular radius of ~9 km at 90 km altitude [*Rosenberg et al.*, 1991]. Because of a variety of performance issues, including the effect of snow accumulation on the riometer's performance [*Rose et al.*, 2000], data were restricted to the period 1999–2001. Data collected during periods of solar proton events were removed and the remaining data corrected for the quiet day curve, including a 0.2 dB offset which occurred in the 2001 data due to a slightly inaccurate quiet day curve. Since the response of the riometer is much stronger in daylight than in darkness, only data taken when Halley was in daylight (October–February) were used. The data were rebinned into 1 min averages as a function of MLT and *AE*, and selected for active magnetic conditions $AE > 300$ nT.

[34] Figure 6 shows the riometer data (middle) in comparison with the previously calculated pitch angle diffusion coefficients (top) and precipitating electron flux (bottom) for active conditions (AE > 300 nT). The riometer absorption shows the same general trend as both the measured electron precipitation and the pitch angle diffusion rates. It peaks just before dawn and has a minimum near 1800 MLT. The

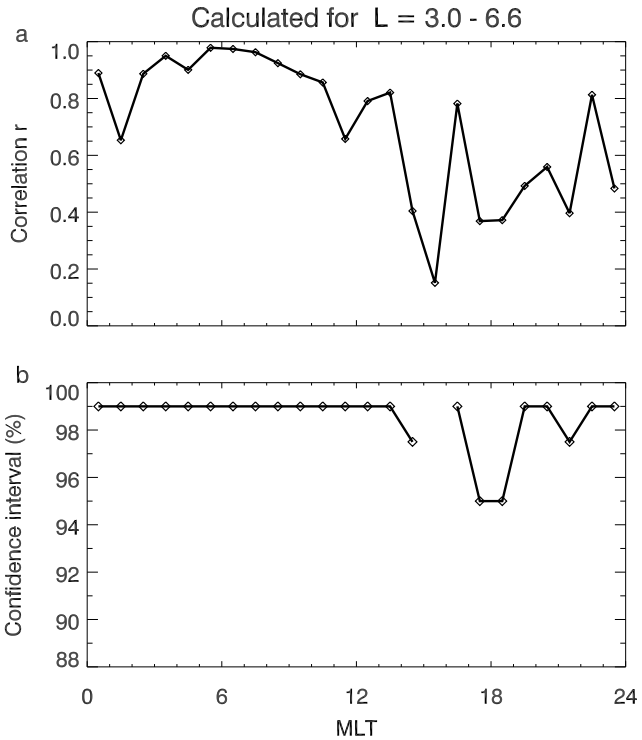

Figure 5. (a) The variation of the Pearson correlation between the log of the $E > 30$ keV precipitating flux and the log of $\langle D_{\alpha\alpha}\rangle_{LC}/p^2$ for lower-band chorus during active conditions over the region $3.0 < L < 6.6$ as a function of MLT and (b) the minimum confidence interval for each correlation.

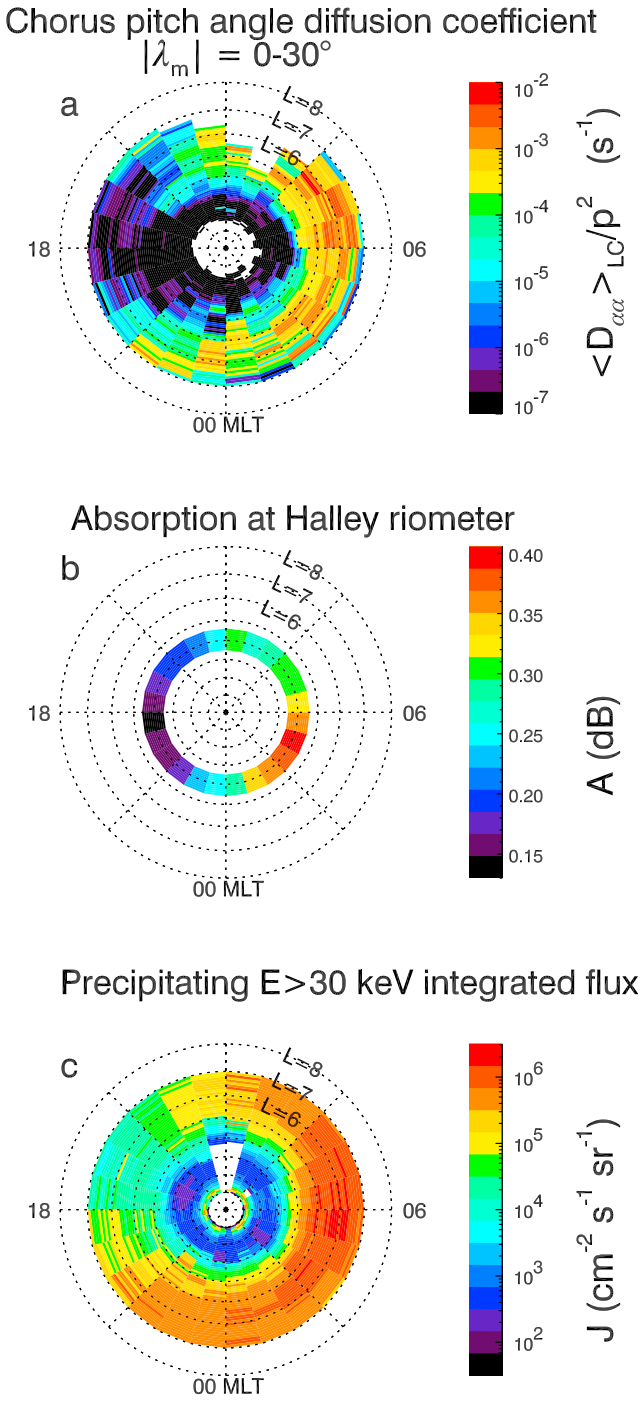

Figure 6. (a) The bounce-averaged pitch angle diffusion coefficient at the edge of the loss cone ($\langle D_{\alpha\alpha}\rangle_{LC}/p^2$) for a combination of equatorial and midlatitude chorus, (b) absorption at the Halley riometer, and (c) the $E > 30$ keV precipitating flux as a function of L and magnetic local time during active conditions (AE > 300 nT).

position of the minimum agrees very well with the pitch angle diffusion coefficients and is in general agreement with the measured precipitating flux. Both satellite and riometer observations suggest that chorus waves near dawn are most effective in causing electron precipitation. This region corresponds to equatorial chorus waves rather than mid latitude chorus, as shown in Figure 3.

7. Discussion

[35] The flux of trapped electrons in Figure 2c falls by approximately an order of magnitude between 0600 MLT and 1200 MLT. The electron flux is controlled by a number of processes in this region, including the supply and transport of electrons via substorms and convective electric fields [e.g., *Lyons et al.*, 2005; *Miyoshi et al.*, 2007], losses to the atmosphere via electron precipitation, and transport out of the region to the dayside. The timescale for transport of 30 keV electrons from the nightside neutral line to noon in the region $4.5 < L < 6.5$ is of the order of a few hours during active conditions [e.g., *Chen and Schulz*, 2001a, 2001b]. If we estimate the electron loss timescales from the reciprocal of the bounce-averaged pitch angle diffusion coefficient at the edge of the loss cone [*Shprits et al.*, 2006] then the loss timescale is of the order of 30 min or so near dawn. This is the timescale for the trapped flux to decay by a factor of e. Since the flux shown in Figure 2c are for constant $L = 5.05$ and we have no detailed information on the drift orbits here we cannot make an exact comparison, but we can at least deduce that electron loss should play an important role in the reduction in >30 keV flux at least near dawn and into the dayside.

[36] The data in Figure 2c show that the precipitating electron flux is at least a factor of 5 lower than the trapped flux, on average, during active times and therefore the electrons are in weak diffusion. We can use this observation as an independent check on calculated pitch angle diffusion rates. Under strong pitch angle diffusion electrons are diffused across the loss cone in less than a quarter of the electron bounce period and the flux within the loss cone approaches isotropy. The diffusion rates computed in Figure 6a should therefore be less than the strong diffusion rate. The strong diffusion rate is given by [*Schulz*, 1974; *Summers and Thorne*, 2003]

$$D_{SD} = \frac{9.66}{L^4}\left[\frac{4L}{4L-3}\right]^{1/2}\frac{[E(E+2E_0)]^{1/2}}{(E+E_0)} \qquad (5)$$

in s^{-1} where $E_0 = m_0c^2$. The strong diffusion rate varies from $D_{SD} \approx 1.4 \times 10^{-2}$ s^{-1} at $L = 4$ to 1.4×10^{-3} s^{-1} at $L = 7$. Figure 6a shows that the bounce averaged diffusion rates are lower than the strong diffusion rate at $L = 4$, and at $L = 7$, consistent with the data, but may sometimes approach the strong diffusion rate near dawn.

[37] Our results suggest that since >30 keV precipitation is MLT-dependent, NO_x production is also MLT-dependent. The longer the precipitation lasts however the more geographically uniform the production of NO_x will be, provided scattering is strong enough to scatter electrons into the bounce loss cone, as is the case for ~300 keV electrons [*Horne et al.*, 2009]. If precipitation lasts 24 h then we expect NO_x production to have some degree of geographical uniformity.

[38] Precipitating >30 keV electrons tend to produce NO_x at ~95 km and below [see *Rees*, 1989, Figure 3.3.3]. If vertical transport within the polar vortex takes place at a rate

similar to that in the Arctic polar vortex during the winter of 2003–2004 [*Clilverd et al.*, 2007] then it takes three months for NO_x generated at 95 km to descend to the top of the stratosphere (~50 km). This is shorter than the period of darkness in the polar regions so that NOx generated by >30 keV electrons in early to mid winter should reach the stratosphere without undergoing photodissociation. The Arctic vortex of 2003–2004 was a particularly powerful vortex for the northern hemisphere, however it should be noted that the Antarctic polar vortex is generally more pronounced and persistent than the Arctic one.

[39] In the northern hemisphere, the maximum descent rate associated with the polar vortex is not over the pole but at 60° N [*Callaghan and Salby*, 2002; *Clilverd et al.*, 2007; *Randall et al.*, 2006] which corresponds to $L \sim 3$–8 (and a mean L of 4.3). We have shown that significant >30 keV electron precipitation occurs for $L \sim 4$–7 during active conditions (Figure 1), that is, NO_x generated by such precipitation occurs at latitudes where the polar vortices can have significant downward transport.

[40] There is not a significant hemispherical difference in the >30 keV electron precipitation flux for $L > 3$ [*Baker et al.*, 2001; *Horne et al.*, 2009], however we anticipate a hemispherical difference in the amount of NO_x transported to the stratosphere due to the asymmetry in the strength and persistence of the Arctic and Antarctic polar vortices.

8. Summary and Conclusions

[41] We have built a statistical model of the $E > 30$ keV precipitating flux as a function of L, magnetic local time (MLT), and geomagnetic activity using data from the NOAA POES satellites and compared it to the statistical distribution of lower-band chorus wave intensities observed in the equatorial and mid latitude region of the magnetosphere. We calculated the associated resonant energies and bounce-averaged diffusion coefficients at the edge of the loss cone and performed a correlation analysis to investigate whether lower-band chorus waves could provide the source of >30 keV electron precipitation. Our key results are

[42] 1. The precipitating flux of $E > 30$ keV electrons varies significantly in MLT and increases substantially with geomagnetic activity as measured by the *AE* index. The data suggest that electron precipitation is related to substorm activity.

[43] 2. There is a strong similarity between the distribution of precipitating electrons >30 keV, riometer absorption at Halley, lower-band chorus wave intensity, and bounce-averaged pitch angle diffusion rates at the edge of the loss cone in MLT and L. There is a high correlation between electron precipitation and pitch angle diffusion rates with correlation coefficients as high as $r > 0.8$ for $L > 5.1$. The correlation becomes even higher in MLT reaching $r > 0.95$ near dawn (between 0500 and 0800 MLT).

[44] 3. The trapped electron flux is at least a factor of 5 larger than the precipitating flux suggesting that, on average, there is no evidence for strong pitch angle diffusion into the loss cone. Pitch angle diffusion rates calculated from lower-band chorus wave intensities are also generally less than the strong diffusion rate.

[45] 4. Since >30 keV precipitation is dependent on MLT and geomagnetic activity, NO_x production should also be MLT-dependent and activity-dependent. The longer the precipitation, however the more geographically uniform NO_x production should be.

[46] 5. Significant >30 keV electron precipitation occurs for $L \sim 4$–7 during active conditions. NO_x generated by such precipitation will occur at latitudes where the polar vortices (especially in the southern hemisphere) can have significant downward transport. Such levels of transport should be sufficient to deposit the NO_x from its altitude of generation downward to the stratosphere during the course of a polar winter.

[47] We conclude that a very important mechanism for precipitating ~30 keV electrons from the inner magnetosphere into the atmosphere is via pitch angle scattering by lower-band chorus waves and that on average the process is described by weak pitch angle diffusion and not strong diffusion. The process, which is strongly dependent on magnetic activity, is capable of producing NO_x at locations where it can be transported to altitudes that are low enough to affect stratospheric chemistry.

Appendix A: Removing Proton Contamination From the POES MEPED Electron Measurements

[48] The POES SEM-2 MEPED detectors are intended to measure the flux of both energetic protons and electrons separately with two different sets of telescope detectors. However, numerical simulations as well as experimental tests of the instrument performed by placing the detectors in particle beams show that the instrument does not always correctly separate the two species. Some protons entering the electron telescopes are mistakenly counted as electrons and vice versa. Here we focus on correcting the electron flux measurements by subtracting the contaminating proton flux. Fortunately, a correction is at least possible because the SEM-2 proton telescopes measure the flux of protons within the energy range that will also contaminate the electron telescopes. However, the energy resolution of the proton detectors is coarse making an accurate correction challenging. The goal of the method described here is to define the proton energy spectrum and thus the electron correction as accurately as possible with the limited information available.

[49] Simulations and tests show that the POES measurements of >30 keV, >100 keV, and >300 keV electrons are contaminated by 210–2700 keV protons, 280–2700 keV protons, and 440–2700 keV protons, respectively. Three of the six energy channels sampled by the MEPED proton telescope span these ranges. The p2, p3 and p4 channels measure the flux of protons with energies from 80–240 keV, 240–800 keV, 800–2500 keV, respectively. Unfortunately, these channels do not perfectly bracket the contaminating proton ranges so the correction is not just a simple subtraction of these counts. For example, the >30 keV electron channel is contaminated by protons with energy above 210 keV but the p2 channel begins measuring protons at 80 keV. The counts measured by the p2 channel from only those protons with energy >210 keV will depend heavily on how the flux varies with energy within the 80–240 keV range. Likewise, only some fraction of the counts measured in the p3 channel will contribute to the contamination of the >100 and >300 keV electron measurements. Since the energy spectrum within a given energy channel is not known, it must be assumed.

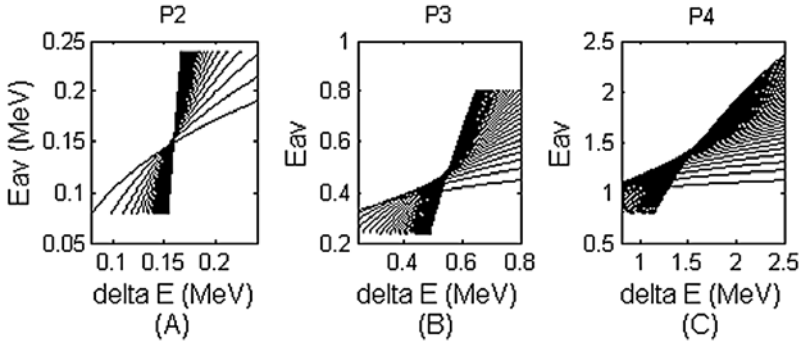

Figure 7. The effect of applying the bow tie analysis of proton data to the electron flux.

[50] We estimate the proton energy spectrum by assuming that it is a series of piecewise exponential functions across each measured proton energy channel range. We define the initial exponential functions using a bow tie method and iterate to improve our knowledge of that spectrum. The bow tie method is defined by *Selesnick and Blake* [2000] and repeated here for completeness.

[51] The total counts measured within an energy band can be defined by

$$C = \int_{E1}^{E2} J(E, \Omega, A, t) dE d\Omega dA dt \tag{A1}$$

where C is the number of counts recorded by the detector during the integration time interval (1 s for the MEPED detectors), $J(E, \Omega, A, t)$ is the differential flux (in cm^{-2} s^{-1} sr^{-1} keV^{-1}) of particles entering the detector, E is the energy of the particle, Ω is solid angle, A is the silicon detector area, and t is time. Assuming that the flux hitting the detector does not vary with the angle of incidence area, or time then integrating gives

$$C = G \int_{E1}^{E2} J(E) dE \tag{A2}$$

where G is the geometric factor. G for the MEPED instrument is .01 cm^{-2} s^{-1} str^{-1}. Now assume that the flux decreases exponentially with energy such that,

$$C = G \int_{E1}^{E2} J_0(E) \exp(-E/E_0) dE \tag{A3}$$

[52] Approximate the integral as the rectangular area with height $J(\tilde{E})$ and width ΔE such that,

$$\begin{aligned} G \int_{E1}^{E2} J_0(E) \exp(-E/E_0) dE &= G J_0 \exp(-\tilde{E}/E_0) \Delta E \\ &= G J(\tilde{E}) \Delta E \end{aligned} \tag{A4}$$

[53] Using the approximation from (9), the counts measured within a given instrument energy band are converted to differential flux by

$$J(\tilde{E}) = \frac{C}{G \Delta E} \tag{A5}$$

[54] The two quantities $\tilde{E}$ and ΔE are related by

$$\Delta E = \exp(-\tilde{E}/E_0) \int_{E1}^{E2} \exp(-E/E_0) dE \tag{A6}$$

and can be plotted as a curve by assuming a fixed E_0. Plotting these curves for different values of E_0 creates a figure that looks like a bow tie. Fixed values of $\tilde{E}$ and ΔE are chosen for each energy band that do not vary much with different assumed spectra. Bow tie plots for the p2, p3 and p4 channels are shown in Figure 7. The values chosen for $\tilde{E}$ for p2, p3 and p4 are 138 keV, 346 keV and 926 keV and the corresponding values of ΔE are 147.9, 345.5, and 461.8 keV. We use these values of $\tilde{E}$ and ΔE to give an initial guess at the proton flux in each energy channel.

[55] To improve our knowledge of the proton flux and energy spectrum we iterate. We calculate new values for E_0 using neighboring flux values. Keeping $\tilde{E}$ fixed, we use equation (A6) and the new values of E_0 to calculate ΔE for each energy channel. We use the new value of ΔE in equation (A5) to define new flux values and repeat the process until the values of E_0 do not change significantly. Lastly, using the piecewise exponential description of the proton energy spectrum we integrate the proton flux from 210–2700 keV, 280–2700 keV, and 440–2700 keV and subtract from the >30, >100 keV and >300 keV electron flux, respectively.

[56] As a final check, Figure 8 shows the integrated precipitating proton flux in the p2 and p3 channels for three levels of geomagnetic activity corresponding to Figure 1. We note that the flux has a different MLT distribution to the electron precipitation shown in Figure 1 and even, for active conditions, the peak average proton precipitation flux is up to 2 orders of magnitude less than the peak average electron precipitation flux. We therefore conclude that after subtracting the proton contamination the error introduced into the electron flux in Figure 1 is small.

Appendix B: Confidence Intervals for Correlation Analysis

[57] In order to quantify whether Pearson correlation values can be considered as significant or not, we calculate percentage confidence intervals for each correlation coefficient. Significant correlations are generally considered to

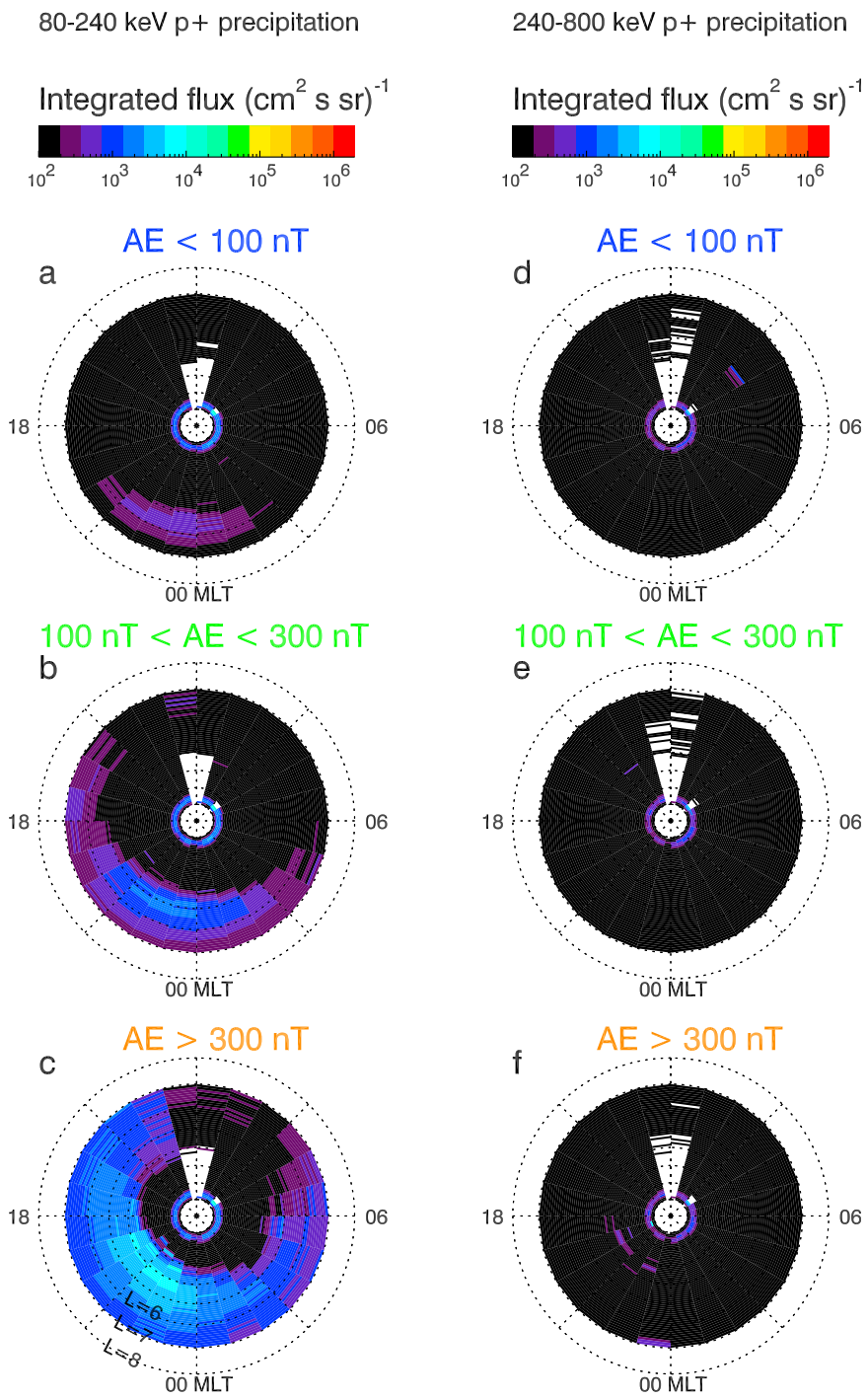

Figure 8. The average flux of precipitating protons for (left) 80–240 keV and (right) 240–800 keV for (a and d) quiet ($AE < 100$ nT), (b and e) moderate ($100 < AE < 300$ nT), and (c and f) active ($AE > 300$ nT) conditions.

have confidence intervals of 95% or above. To do this we calculate the quantity

$$t = \frac{r\sqrt{(N-2)}}{\sqrt{(1-r^2)}} \tag{B1}$$

where r is the Pearson's correlation and N is the number of pairs of scores that went into the computation of r. Then we determine whether each Pearson coefficient was equal to or exceeded the 90%, 95%, 97.5% or 100% confidence interval using look-up tables of critical two-tailed values of t for these confidence intervals. We plot minimum confidence levels (only for confidence levels of at least 90%) in Figures 4b and 5b.

[58] **Acknowledgments.** We would like to thank Roger R. Anderson for the provision of the wave data, Hannah Vickers and Bob Weigel for assistance with processing the NOAA POES data, Craig Roger for discussions about NOAA POES data set, Nicola Longden and Mark Clilverd for discussions about riometer data, and the NSSDC Omniweb for providing the geomagnetic indices. This work was supported by the Natural Environment Research Council.

[59] Wolfgang Baumjohann thanks the reviewers for their assistance in evaluating 2009JA014619.

References

Albert, J. M., N. P. Meredith, and R. B. Horne (2009), Three-dimensional diffusion simulation of outer radiation belt electrons during the 9 October 1990, magnetic storm, *J. Geophys. Res.*, *114*, A09214, doi:10.1029/2009JA014336.

Anderson, R. R., D. A. Gurnett, and D. L. Odem (1992), CRRES plasma wave experiment, *J. Spacecr. Rockets*, *29*, 570.

Baker, D., C. Barth, K. Mankoff, S. Kanekal, S. Bailey, G. Mason, and J. Mazur (2001), Relationships between precipitating auroral zone electrons and lower thermospheric nitric oxide densities: 1998–2000, *J. Geophys. Res.*, *106*, 24,465–24,480.

Blake, J. B., M. D. Looper, D. N. Baker, R. Nakamura, B. Klecker, and D. Hovestadt (1996), New high temporal and spatial resolution measurements by SAMPEX of the precipitation of relativistic electrons, *Adv. Space. Res.*, *18*(8), 171–186.

Bortnik, J., R. M. Thorne, T. P. O'Brien, J. C. Green, R. J. Strangeway, Y. Y. Shprits, and D. N. Baker (2006), Observation of two distinct, rapid loss mechanisms during the 20 November 2003 radiation belt dropout event, *J. Geophys. Res.*, *111*, A12216, doi:10.1029/2006JA011802.

Callaghan, P. F., and M. L. Salby (2002), Three-dimensionality and forcing of the Brewer-Dobson circulation, *J. Atmos. Sci.*, *59*(5), 976–991.

Chen, M., and M. Schulz (2001a), Simulations of storm time diffuse aurora with plasma sheet electrons in strong pitch angle diffusion, *J. Geophys. Res.*, *106*, 1873–1886.

Chen, M., and M. Schulz (2001b), Simulations of diffuse aurora with plasma sheet electrons in pitch angle diffusion less than everywhere strong, *J. Geophys. Res.*, *106*, 28,949–28,966.

Clilverd, M. A., A. Seppälä, C. J. Rodger, N. R. Thomson, J. Lichtenberger, and P. Steinbach (2007), Temporal variability of the descent of high-altitude NOx inferred from ionospheric data, *J. Geophys. Res.*, *112*, A09307, doi:10.1029/2006JA012085.

Clilverd, M. A., A. Seppälä, C. J. Rodger, M. G. Mlynczak, and J. U. Kozyra, (2009), Additional stratospheric NOx production by relativistic electron precipitation during the 2004 spring NOx descent event, *J. Geophys. Res.*, *114*, A04305, doi:10.1029/2008JA013472.

Codrescu, M. V., T. J. Fuller-Rowell, R. G. Roble, and D. S. Evans (1997), Medium energy particle precipitation influences on the mesosphere and lower thermosphere, *J. Geophys. Res.*, *102*, 19,977–19,987.

Collis, P. N., J. K. Hargreaves, and A. Korth (1984), Auroral radio absorption as an indicator of magnetospheric electrons and of conditions in the disturbed auroral D-region, *J. Atmos. Terr. Phys.*, *46*, 21–38.

Foat, J., R. Lin, D. Smith, F. Fenrich, R. Millan, I. Roth, K. Lorentzen, M. McCarthy, G. Parks, and J. Treilhou (1998), First detection of a terrestrial MeV X-Ray burst, *J. Geophys. Res.*, *25*, 4109–4112.

Fok, M.-C., R. B. Horne, N. P. Meredith, and S. A. Glauert (2008), Radiation belt environment model: Application to space weather nowcasting, *J. Geophys. Res.*, *113*, A03S08, doi:10.1029/2007JA012558.

Fuller-Rowell, T. J., and D. S. Evans (1987), Height-integrated Pedersen and Hall conductivity patterns inferred from the TIROS-NOAA Satellite Data, *J. Geophys. Res.*, *92*, 7606–7618.

Gaines, E. E., D. L. Chenette, W. L. Imhof, C. H. Jackman, and J. D. Winningham (1995), Relativistic electron fluxes in May 1992 and their effect on the middle atmosphere, *J. Geophys. Res.*, *100*, 1027–1033.

Glauert, S. A., and R. B. Horne (2005), Calculation of pitch angle and energy diffusion coefficients with the PADIE code, *J. Geophys. Res.*, *110*, A04206, doi:10.1029/2004JA010851.

Hardy, D. A., E. G. Holeman, W. J. Burke, L. C. Gentile, and K. H. Bounar (2008), Probability distributions of electron precipitation at high magnetic latitudes, *J. Geophys. Res.*, *113*, A06305, doi:10.1029/2007JA012746.

Hargreaves, J. K. (1979), *The Upper Atmosphere and Solar-Terrestrial Relations*, Van Nostrand Reinhold, New York.

Horne, R. B., and R. M. Thorne (1998), Potential waves for relativistic electron scattering and stochastic acceleration during magnetic storms, *Geophys. Res. Lett.*, *25*, 3011–3014.

Horne, R. B., and R. M. Thorne (2000), Electron pitch angle diffusion by electrostatic electron cyclotron harmonic waves: the origin of pancake distributions, *J. Geophys. Res.*, *105*, 5391–5402.

Horne, R. B., P. J. Christiansen, and M. P. Gough (1987), Weak electrostatic waves near the upper hybrid frequency: A comparison between theory and experiment, *J. Geophys. Res.*, *92*, 3243–3259.

Horne, R. B., R. M. Thorne, S. A. Glauert, J. M. Albert, N. P. Meredith, and R. R. Anderson (2005), Timescale for radiation belt electron acceleration by whistler mode chorus waves, *J. Geophys. Res.*, *110*, A03225, doi:10.1029/2004JA010811.

Horne, R. B., R. M. Thorne, S. A. Glauert, N. P. Meredith, D. Pokhotelov, and O. Santolík (2007), Electron acceleration in the Van Allen radiation belts by fast magnetosonic waves, *Geophys. Res. Lett.*, *34*, L17107, doi:10.1029/2007GL030267.

Horne, R. B., M. M. Lam, and J. C. Green (2009), Energetic electron precipitation from the outer radiation belt during geomagnetic storms, *Geophys. Res. Lett.*, *36*, L19104, doi:10.1029/2009GL040236.

Inan, U. S., Y. T. Chiu, and G. T. Davidson (1992), Whistler-mode chorus and morning-side aurorae, *Geophys. Res. Lett.*, *19*, 653–656.

Inan, U. S., D. Piddyachiy, W. B. Peter, J. A. Sauvaud, and M. Parrot (2007), DEMETER satellite observations of lightning-induced electron precipitation, *Geophys. Res. Lett.*, *34*, L07103, doi:10.1029/2006GL029238.

Johnson, M. H., and J. Kierein (1992), Combined Release and Radiation Effects Satellite (CRRES): Spacecraft and mission, *J. Spacecr. Rockets*, *29*, 556–563.

Johnstone, A. D., D. M. Walton, R. Liu, and D. A. Hardy (1993), Pitch angle diffusion of low-energy electrons by whistler mode waves, *J. Geophys. Res.*, *98*, 5959–5967.

Jordanova, V. K., J. Albert, and Y. Miyoshi (2008), Relativistic electron precipitation by EMIC waves from self-consistent global simulations, *J. Geophys. Res.*, it 113, A00A10, doi:10.1029/2008JA013239.

Kozyra, J. U., et al. (2006), Response of the upper/middle atmosphere to coronal holes and powerful high-speed solar wind streams in 2003, in *Co-Rotating Solar Wind Streams and Recurrent Geomagnetic activity*, *Geophys. Monogr. Ser.*, vol 167, edited by B. T. Tsurutani et al., pp. 319–340, AGU, Washington, D. C.

Lorentzen, K., M. McCarthy, G. Parks, J. Foat, R. Millan, D. Smith, R. Lin, and J. Treilhou (2000), Precipitation of relativistic electrons by interaction with electromagnetic ion cyclotron waves, *J. Geophys. Res.*, *105*, 5381–5389.

Lorentzen, K., J. Blake, U. Inan, and J. Bortnik (2001a), Observations of relativistic electron microbursts in association with VLF chorus, *J. Geophys. Res.*, *106*, 6017–6027.

Lorentzen, K., M. Looper, and J. Blake (2001b), Relativistic electron microbursts during the GEM Storms, *Geophys. Res. Lett.*, *28*, 2573–2576.

Lyons, L. R., D.-Y. Lee, R. M. Thorne, R. B. Horne, and A. J. Smith (2005), Solar-wind magnetosphere coupling leading to relativistic electron energization during high-speed streams, *J. Geophys. Res.*, *110*, A11202, doi:10.1029/2005JA011254.

Meredith, N. P., R. B. Horne, and R. R. Anderson (2001), Substorm dependence of chorus amplitudes: Implications for the acceleration of electrons to relativistic energies, *J. Geophys. Res.*, *106*, 13,165–13,178.

Meredith, N. P., R. B. Horne, D. Summers, R. M. Thorne, R. H. A. Iles, D. Heynderickx, and R. R. Anderson (2002), Evidence for acceleration of outer zone electrons to relativistic energies by whistler mode chorus, *Ann Geophys.*, *20*(7), 967–979.

Meredith, N. P., M. Cain, R. B. Horne, R. M. Thorne, D. Summers, and R. R. Anderson (2003), Evidence for chorus driven electron acceleration to relativistic energies from a survey of geomagnetically disturbed periods, *J. Geophys. Res.*, *108*(A6), 1248, doi:10.1029/2002JA009764.

Meredith, N. P., R. B. Horne, R. M. Thorne, D. Summers, and R. R. Anderson (2004), Substorm dependence of plasmaspheric hiss, *J. Geophys. Res.*, *109*, A06209, doi:10.1029/2004JA010387.

Millan, R. M., and R. M. Thorne (2007), Review of radiation belt relativistic electron losses, *J. Atmos. Terr. Phys.*, *69*, 362–377, doi:10.1016/jastp.2006.06.019.

Millan, R. M., R. P. Lin, D. M. Smith, K. R. Lorentzen, and M. P. McCarthy (2002), X-ray observations of MeV electron precipitation with a balloon-borne germanium spectrometer, *Geophys. Res. Lett.*, *29*(24), 2194, doi:10.1029/2002GL015922.

Miyoshi, Y., A. Morioka, T. Obara, H. Misawa, T. Nagai, and Y. Kasahara (2003), Rebuilding process of the outer radiation belt during the 3 November 1993 magnetic storm: NOAA and Exos-D observations, *J. Geophys. Res.*, *108*(A1), 1004, doi:10.1029/2001JA007542.

Miyoshi, Y., A. Morioka, R. Kataoka, Y. Kasahara, and T. Mukai (2007), Evolution of the outer radiation belt during the November 1993 storms driven by corotating interaction regions, *J. Geophys. Res.*, *112*, A05210, doi:10.1029/2006JA012148.

Miyoshi, Y., K. Sakaguchi, K. Shiokawa, D. Evans, J. Albert, M. Connors, and V. Jordanova (2008), Precipitation of radiation belt electrons by EMIC waves, observed from ground and space, *Geophys. Res. Lett.*, *35*, L23101, doi:10.1029/2008GL035727.

Newell, P. T., K. M. Lyons, and C.-I. Meng (1996a), A large survey of electron acceleration events, *J. Geophys. Res.*, *101*, 2599–2614.

Newell, P. T., Y. I. Feldstein, Y. I. Galperin, and C.-I. Meng (1996b), Morphology of nightside precipitation, *J. Geophys. Res.*, *101*, 10,737–10,748.

Ni, B., R. M. Thorne, Y. Y. Shprits, and J. Bortnik (2008), Resonant scattering of plasma sheet electrons by whistler-mode chorus: Contribution to diffuse auroral precipitation, *Geophys. Res. Lett.*, *35*, L11106, doi:10.1029/2008GL034032.

O'Brien, T. P., and R. L. McPherron (2003), An empirical dynamic equation for energetic electrons at geosynchronous orbit, *J. Geophys. Res.*, *108*(A3), 1137, doi:10.1029/2002JA009324.

O'Brien, T. P., M. D. Looper, and J. B. Blake (2004), Quantification of relativistic electron microburst losses during the GEM storms, *Geophys. Res. Lett.*, *31*, L04802, doi:10.1029/2003GL018621.

Olson, W. P., and K. Pfitzer (1977), Magnetospheric magnetic field modelling, annual scientific report, AFOSR contract F44620-75-c-0033, Air Force Off. of Sci. Res., Arlington, Va.

Omura, Y., N. Furuya, and D. Summers (2007), Relativistic turning acceleration of resonant electrons by coherent whistler mode waves in a dipole magnetic field, *J. Geophys. Res.*, *112*, A06236, doi:10.1029/2006JA012243.

Parks, G. K. (1978), Microburst precipitation phenomena, *J. Geomagn. Geoelectr.*, *30*, 327–341.

Randall, C. E., et al. (2005), Stratospheric effects of energetic particle precipitation in 2003–2004, *Geophys. Res. Lett.*, *32*, L05802, doi:10.1029/2004GL022003.

Randall, C. E., V. L. Harvey, C. S. Singleton, P. F. Bernath, C. D. Boone, and J. U. Kozyra (2006), Enhanced NOx in 2006 linked to strong upper stratospheric Arctic vortex, *Geophys. Res. Lett.*, *33*, L18811, doi:10.1029/2006GL027160.

Rees, M. H. (1989), *Physics and Chemistry of the Upper Atmosphere*, Cambridge Univ. Press, Cambridge, U. K.

Roble, R. G., and E. C. Ridley (1987), An auroral model for the NCAR thermospheric general circulation model (TGCM), *Ann. Geophys.*, *5A*(6), 369–382.

Rodger, C. J., M. A. Clilverd, J. C. Green, and M. M. Lam (2010), Use of POES SEM-2 observations to examine radiation belt dynamics and energetic electron precipitation into the atmosphere, *J. Geophys. Res.*, doi:10.1029/2008JA014023, in press.

Rose, M. C., M. J. Jarvis, M. A. Clilverd, D. J. Maxfield, and T. J. Rosenberg (2000), The effect of snow accumulation on imaging riometer performance, *Radio Sci.*, *35*, 1143–1153.

Rosenberg, T. J., and J. R. Dudeney (1986), The local time, substorm, and seasonal dependence of electron-precipitation at L = 4 inferred from riometer measurements, *J. Geophys. Res.*, *91*, 12,032–12,040.

Rosenberg, T. J., D. L. Detrick, D Venkatesan, and G Vanbavel (1991), A comparative study of imaging and broadbeam riometer measurements: the effect of spatial structure on the frequency dependence of auroral absorption, *J. Geophys. Res.*, *96*, 17,793–17,803.

Rozanov, E., L. Callis, M. Schlesinger, F. Yang, N. Andronova, and V. Zubov (2005), Atmospheric response to NOy source due to energetic electron precipitation, *Geophys. Res. Lett.*, *32*, L14811, doi:10.1029/2005GL023041.

Santolík, O., D. A. Gurnett, J. S. Pickett, M. Parrot, and N. Cornilleau-Wehrlin (2004), A microscopic and nanoscopic view of storm-time chorus on 31 March 2001, *Geophys. Res. Lett.*, *31*, L02801, doi:10.1029/2003GL018757.

Schulz, M. (1974), Particle lifetimes in strong diffusion, *Astrophys. Space Sci.*, *31*, 37–42.

Selesnick, R., and J. Blake (2000), On the source location of radiation belt relativistic electrons, *J. Geophys. Res.*, *105*, 2607–2624.

Shprits, Y. Y., W. Li, and R. M. Thorne (2006), Controlling effect of the pitch angle scattering rates near the edge of the loss cone on electron lifetimes, *J. Geophys. Res.*, *111*, A12206, doi:10.1029/2006JA011758.

Siskind, D. E., G. E. Nedoluha, C. E. Randall, M. Fromm, and J. M. Russell III (2000), An assessment of southern hemisphere stratospheric NO_x enhancements due to transport from the upper atmosphere, *Geophys. Res. Lett.*, *27*, 329–332.

Solomon, S., P. J. Crutzen, and R. G. Roble (1982), Photochemical coupling between the thermosphere and the lower atmosphere: 1. Odd nitrogen from 50 to 120 km, *J. Geophys. Res.*, *87*, 7206–7220.

Summers, D., and R. M. Thorne (2003), Relativistic electron pitch angle scattering by electromagnetic ion cyclotron waves during geomagnetic storms, *J. Geophys. Res.*, *108*(A4), 1143, doi:10.1029/2002JA009489.

Summers, D., B. Ni, N. P. Meredith, R. B. Horne, R. M. Thorne, M. B. Moldwin, and R. R. Anderson (2008), Electron scattering by whistler-mode ELF hiss in plasmaspheric plumes, *J. Geophys. Res.*, *113*, A04219, doi:10.1029/2007JA012678.

Thorne, R. M. (1977), Energetic radiation belt electron precipitation: a natural depletion mechanism for stratospheric ozone, *Science*, *195*, 287–289.

Thorne, R. M., T. P. O'Brien, Y. Y. Shprits, D. Summers, and R. B. Horne (2005), Timescale for MeV electron microburst loss during geomagnetic storms, *J. Geophys. Res.*, *110*, A09202, doi:10.1029/2004JA010882.

Tsurutani, B. T., and E. J. Smith (1974), Postmidnight chorus: A substorm phenomenon, *J. Geophys. Res.*, *79*, 118–127.

Tsurutani, B. T., and E. J. Smith (1977), Two types of magnetospheric ELF chorus and their substorm dependencies, *J. Geophys. Res.*, *82*, 5112–5128.

Varotsou, A., D. Boscher, S. Bourdarie, R. B. Horne, S. A. Glauert, and N. P. Meredith (2005), Simulation of the outer radiation belt electrons near geosynchronous orbit including both radial diffusion and resonant interaction with whistler-mode chorus waves, *Geophys. Res. Lett.*, *32*, L19106, doi:10.1029/2005GL023282.

Varotsou, A., D. Boscher, S. Bourdarie, R. B. Horne, N. P. Meredith, S. A. Glauert, and R. H. Friedel (2008), Three-dimensional test simulations of the outer radiation belt electron dynamics including electron-chorus resonant interactions, *J. Geophys. Res.*, *113*, A12212, doi:10.1029/2007JA012862.

Voss, H. D., et al. (1984), Lightning-induced electron precipitation, *Nature*, *312*, 740–742.

Voss, H., M. Walt, W. Imhof, J. Mobilia, and U. Inan (1998), Satellite observations of lightning-induced electron precipitation, *J. Geophys. Res.*, *103*, 11,725–11,744.

Walker, A. D. M. (1993), *Plasma Waves in the Magnetosphere*, Springer, New York.

S. A. Glauert, R. B. Horne, N. P. Meredith, and T. Moffat-Griffin, British Antarctic Survey, Natural Environment Research Council, Madingley Road, Cambridge CB3 0ET, U. K. (sagl@bas.ac.uk; rh@bas.ac.uk; nmer@bas.ac.uk; tmof@bas.ac.uk)

J. C. Green, Space Weather Prediction Center, National Oceanic and Atmospheric Administration, 325 Broadway Blvd., Boulder, CO 80305-0000, USA. (janet.green@noaa.gov)

M. M. Lam, Department of Physics and Astronomy, University of Leicester, University Road, Leicester LE1 7RH, U. K. (mml9@ion.le.ac.uk)